J. Fluid Mech. (2014), *vol.* 744, *pp.* 376–403.
doi:10.1017/jfm.2014.82

On the onset of wake meandering for an axial flow turbine in a turbulent open channel flow

Seokkoo Kang[1,2], Xiaolei Yang[1] and Fotis Sotiropoulos[1,†]

[1]St. Anthony Falls Laboratory, Department of Civil Engineering, University of Minnesota, 2 Third Avenue SE, Minneapolis, MN 55414, USA

[2]Department of Civil and Environmental Engineering, Hanyang University, Seoul 133-791, Republic of Korea

(Received 28 March 2013; revised 5 December 2013; accepted 6 February 2014)

Laboratory experiments have yielded evidence suggestive of large-scale meandering motions in the wake of an axial flow hydrokinetic turbine in a turbulent open channel flow (Chamorro *et al.*, *J. Fluid Mech.*, vol. 716, 2013, pp. 658–670). We carry out a large-eddy simulation (LES) of the experimental flow to investigate the structure of turbulence in the wake of the turbine and elucidate the mechanism that gives rise to wake meandering. All geometrical details of the turbine structure are taken into account in the simulation using the curvilinear immersed boundary LES method with wall modelling (Kang *et al.*, *Adv. Water Resour.*, vol. 34(1), 2011, pp. 98–113). The simulated flow fields are in good agreement with the experimental measurements and confirm the theoretical model of turbine wakes (Joukowski, *Tr. Otdel. Fizich. Nauk Obshch. Lyub. Estestv.*, vol. 16, 1912, no. 1), yielding a near-turbine wake that consists of two layers: the tip vortex (or outer) shear layer that rotates in the same direction as the rotor; and the inner layer counter-rotating hub vortex. Analysis of the calculated instantaneous flow fields reveals that the hub vortex undergoes spiral vortex breakdown and precesses slowly in the direction opposite to the turbine rotation. The precessing vortex core remains coherent for three to four rotor diameters, expands radially outwards, and intercepts the outer shear layer at approximately the location where wake meandering is initiated. The wake meandering manifests itself in terms of an elongated region of increased turbulence kinetic energy and Reynolds shear stress across the top tip wake boundary. The interaction of the outer region of the flow with the precessing hub vortex also causes the rotational component of the wake to decay completely at approximately the location where the wake begins to meander (four rotor diameters downstream of the turbine). To further investigate the importance of turbine geometry on far-wake dynamics, we carry out LES under the same flow conditions but using actuator disk and actuator line parametrizations of the turbine. While both actuator approaches yield a meandering wake, the actuator line model yields results that are in better overall agreement with the measurements. However, comparisons between the actuator line and the turbine-resolving LES reveal significant differences. Namely, in the actuator line LES model: (i) the hub vortex does not develop spiral instability and remains stable and columnar without ever intercepting the outer shear layer; (ii) wake rotation persists for much longer distance downstream than in the turbine-resolving LES; and (iii) the level of turbulence kinetic energy within and the overall size of the far-wake meandering region are considerably

† Email address for correspondence: fotis@umn.edu

smaller (this discrepancy is even more pronounced for the actuator disk LES case) compared with the turbine-resolving LES. Our results identify for the first time the instability mechanism that amplified wake meandering in the experiment of Chamorro *et al.*, show that computational models that do not take into account the geometrical details of the turbine cannot capture such phenomena, and point to the potential significance of the near-hub rotor design as a means for suppressing the instability of the hub vortex and diminishing the extent and intensity of the far-wake meandering region.

Key words: turbulent flows, turbulence simulation

1. Introduction

Hydrokinetic turbines can be used to harness energy from tides, rivers and streams without requiring a dam to impound the water. Because of their potential as a significant contributor to renewable energy generation, such devices are currently being deployed with increasing frequency in waterways (Güney & Kaygusuz 2010; Chamorro *et al.* 2013*a*,*b*). Future deployments are expected to involve multi-turbine arrays with the aim to produce megawatt-scale electricity. The success of such deployments hinges on understanding the structure of turbine wakes and their potential interactions with neighbouring turbines in an array as well as the interaction of turbine-induced coherent motions with the aquatic environment.

This paper is motivated by the recent work of Chamorro *et al.* (2013*a*), who studied experimentally the interaction of a fully developed turbulent flow with a typical axial flow hydrokinetic turbine mounted on the bed of an open channel. A major finding of their work is that the turbine wake is stable at distances less than three rotor diameters but further downstream it starts exhibiting intense low-frequency lateral motions. Chamorro *et al.* (2013*a*) attributed this feature of the wake to the onset of wake meandering, a phenomenon that has also been shown to occur in wind turbine wakes (Medici & Alfredsson 2008). Owing to limitations inherent in laboratory measurements of such a complex three-dimensional flow, however, Chamorro *et al.* (2013*a*) could neither visualize this large-scale flow instability nor explain its origin. Most previous turbine wake studies have focused primarily on developing simple wake models for wind turbines that can reproduce the effects of low-frequency wake meandering as a function of the inflow conditions (Larsen *et al.* 2008). A few studies have also attempted to examine the underlying mechanisms of wake instability using theoretical, experimental or numerical approaches. Okulov & Sørenson (2007), for instance, carried out theoretical stability analysis of the helical tip vortices and the hub vortices behind a turbine. They showed that the radial extent of the hub vorticity affects the stability of the blade tip vortices and that the wake consisting of the helical tip vortices and a hub vortex is unconditionally unstable. Their study, however, was restricted to idealized inviscid flow with steady and uniform inflow velocity field. Ivanell *et al.* (2010), on the other hand, studied the stability of the tip vortices by carrying out large-eddy simulation (LES) using the actuator line method for parametrizing the turbine blades. They reported the occurrence of vortex pairing during the development of the instability of the tip vortices. It is, however, not clear from this study whether or not the tip vortex instability leads to the instability of the entire wake (i.e. wake meandering). Furthermore, this study only considered idealized inflow conditions, assuming steady, laminar and uniform incoming flow, and thus

could not examine the effect of ambient turbulence on the dynamics of the turbine wake. More recently, Espana *et al.* (2011) measured experimentally the width of the wake behind a model turbine consisting of a porous disk. They reported that wake meandering occurs when the incoming turbulence length scale is larger than the wake width, and the size of the mean wake is highly affected by the meandering process. This study approximated the turbine as a porous disk, following the actuator disk concept (Glauert 1935), but the influence of such an approximation on the wake meandering revealed by the experiment could not be investigated.

The above literature review points to the conclusion that simplified approximations of axial turbines as actuator disks (AD) or rotating actuator lines (AL) are sufficient to produce wake instability under both steady uniform inflow and more realistic turbulent inflow conditions. The mechanism that leads to such instability, however, is not yet clearly understood. For instance, the fact that an actuator disk representation of the turbine produces wake meandering (as found by Espana *et al.* 2011) suggests that instability of the helical tip vortices (Ivanell *et al.* 2010), which could only arise in AL models or real-life turbines, is neither a critical prerequisite nor a unique mechanism for giving rise to far-wake instability. Most importantly, previous studies have implicitly assumed that the wake structure predicted by models based on simplified approximations of the turbine geometry provides a good approximation to the wake arising in realistic turbine geometries. Such an assumption has indeed been supported by a number of recent studies using AD or AL turbine models, which have yielded results in reasonable agreement with wind tunnel measurements (Wu & Porté-Agel 2011; Aubrun *et al.* 2012). The agreement between measurements and simulations in these studies has been found to improve in the far-wake region where one would reasonably anticipate that specific effects of the turbine geometry diminish (Aubrun *et al.* 2012). However, the precise relationship between the three-dimensional structure and overall dynamics of the wake that arises in actuator-type turbine models to that arising in realistic turbine geometries has yet to be investigated systematically.

In this work, we carry out turbine-geometry-resolving LES (LES-TR) of the flow studied experimentally by Chamorro *et al.* (2013*a*) to elucidate the three-dimensional wake structure of a real-life hydrokinetic turbine and to reveal possible mechanisms of the wake instability. We employ the curvilinear immersed boundary approach with wall modelling (Kang *et al.* 2011, 2012) to take into account all geometrical details of the turbine and resolve the interaction of its rotating and stationary components with the incoming turbulent flow and the open channel walls. The simulated flow fields are compared with the experimental measurements of Chamorro *et al.* (2013*a*) in terms of mean flow velocity profiles and turbulent statistics, and shown to be in very good agreement. Subsequently, we analyse the simulated flow fields to elucidate the three-dimensional structure of the wake and uncover the mechanism that gives rise to wake meandering for this case. To systematically investigate the effect of simplified turbine parametrizations on wake structure and help to interpret the findings of the LES-TR, we also carry out LES with AD and AL models (LES-AD and LES-AL, respectively) for identical flow conditions as for the LES-TR case. We show that the AD and AL models give rise to three-dimensional wake structure and meandering dynamics that exhibit significant differences with the wake predicted by LES-TR. The most striking finding in this regard is that, in addition to the anticipated differences in the near-wake region, differences between the actuator-type models and the LES-TR persist for many diameters downstream of the turbine. We show that this finding is due to the fact that for the LES-TR case the wake meandering mechanism appears to be linked to a large-scale low-frequency instability of the flow that originates immediately downstream of

the turbine hub and manifests itself as a slowly precessing spiral hub vortex. Such instability depends on the geometrical details of the near-hub region of the turbine geometry and naturally cannot be predicted by either AL or AD models.

This paper is organized as follows. In § 2 we describe the computational model of Kang *et al.* (2012). In § 3 we describe the flume experiments of Chamorro *et al.* (2013*a*) and present the details of numerical simulations. Subsequently, in § 4 we present and analyse the LES-TR, LES-AD and LES-AL results, compare them with laboratory experiments, and analyse the physics of the turbine wake. In § 5 we present the conclusions of this study and discuss areas for future research.

2. Numerical methods

For the turbine-geometry-resolving simulations (LES-TR), we employ LES coupled with the curvilinear immersed boundary (CURVIB) method (Kang *et al.* 2011) to effectively handle arbitrarily complex geometries with moving boundaries. The CURVIB-LES approach was first introduced by Kang *et al.* (2011) and has been successfully applied to simulate a wide range of turbulent flows involving complex moving and stationary bodies, which include turbulent flow in real-life meandering streams (Kang *et al.* 2011; Kang & Sotiropoulos 2011, 2012*a*), turbulent free-surface flow (Kang & Sotiropoulos 2012*b*), sediment transport in open channels (Khosronejad *et al.* 2011; Khosronejad, Kang & Sotiropoulos 2012; Khosronejad *et al.* 2013) and turbulent flow past a hydrokinetic turbine (Kang *et al.* 2012).

The equations governing the instantaneous flow field for LES of incompressible turbulent flow are the three-dimensional spatially averaged continuity and Navier–Stokes equations. In the hybrid staggered/non-staggered curvilinear grid formulation used in the CURVIB method (Ge & Sotiropoulos 2007), the governing equations are first written in Cartesian coordinates $\{x_i\}$ and then fully transformed (both the velocity vector and spatial coordinates are expressed in curvilinear coordinates) in non-orthogonal generalized curvilinear coordinates $\{\xi^i\}$. The transformed equations read in compact tensor notation (repeated indices imply summation) as follows $(i, j = 1, 2, 3)$:

$$J\frac{\partial U^j}{\partial \xi^j} = 0, \tag{2.1}$$

$$\frac{1}{J}\frac{\partial U^i}{\partial t} = \frac{\xi_l^i}{J}\left(-\frac{\partial}{\partial \xi^j}(U^j u_i) + \frac{1}{\rho}\frac{\partial}{\partial \xi^j}\left(\mu\frac{g^{jk}}{J}\frac{\partial u_i}{\partial \xi^k}\right) - \frac{1}{\rho}\frac{\partial}{\partial \xi^j}\left(\frac{\xi_i^j p}{J}\right) - \frac{1}{\rho}\frac{\partial \tau_{ij}}{\partial \xi^j} + F_l\right), \tag{2.2}$$

where $J = |\partial(\xi^1, \xi^2, \xi^3)/\partial(x_1, x_2, x_3)|$ is the Jacobian of the geometric transformation, $\xi_j^i = \partial \xi^i/\partial x_j$ are the transformation metrics, u_i is the filtered ith Cartesian velocity component, $U^i = (\xi_m^i/J)u_m$ is the filtered contravariant volume flux, $g^{jk} = \xi_l^j \xi_l^k$ are the components of the contravariant metric tensor, p is the filtered pressure, ρ is the density, μ is the dynamic viscosity, τ_{ij} is the sub-grid stress (SGS) tensor for LES, and F_l is a body force used to account for the presence of the turbine in the flow for actuator-type models. For LES-TR this force is set equal to zero since the details of the turbine geometry are resolved using the CURVIB method. The approaches we employ to calculate and prescribe this force in LES-AD and LES-AL will be discussed later in this section. The SGS terms are modelled using the Smagorinsky model (Smagorinsky 1963)

$$\tau_{ij} - \frac{1}{3}\tau_{kk}\delta_{ij} = -2\mu_t \overline{S_{ij}}, \tag{2.3}$$

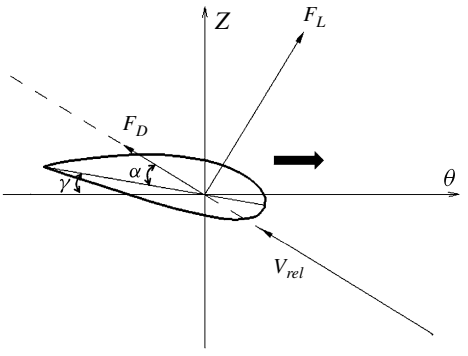

FIGURE 1. Schematic of a 2D foil element for the AL model, in which L and D are the lift and drag, respectively, α is the angle of attack, γ is the angle of blade pitch, and V_{rel} is the relative incoming velocity to the foil. The blade rotates from left to right on this plane.

where the overbar denotes the grid filtering operation, and $\overline{S_{ij}}$ is the filtered strain-rate tensor. The eddy viscosity is given by

$$\mu_t = \rho C_s \Delta^2 |\overline{S}|, \tag{2.4}$$

where C_s is the Smagorinsky constant, Δ is the filter size and $|\overline{S}| = \sqrt{2\overline{S_{ij}}\,\overline{S_{ij}}}$. The filter size is taken as the cube root of the cell volume. The Smagorinsky constant (C_s) is computed using the dynamic Smagorinsky model (Germano *et al.* 1991) implemented in the context of the CURVIB method (Kang *et al.* 2011).

The AD and AL models are employed for the LES with turbine parametrization. These models have recently been employed quite extensively to study wind turbine wakes (Ivanell *et al.* 2009, 2010; Calaf, Meneveau & Meyers 2010; Espana *et al.* 2011; Yang, Kang & Sotiropoulos 2012). In the AD model, the turbine rotor is represented by a permeable circular disk with uniformly distributed thrust forces. The details of the specific implementation of LES-AD in this work can be found in Yang *et al.* (2012). The AL model (Sørensen & Shen 2002), on the other hand, accounts for the blades as separate rotating lines. The forces distributed on each line (blade) are calculated based on a blade element approach, in which the blade is divided into elements in the radial direction, using tabulated 2D foil data. As shown in figure 1, the lift (F_L) and drag (F_D) forces on each element are calculated as

$$F_{L,D} = \frac{1}{2}\rho C_{L,D} C V_{rel}^2, \tag{2.5}$$

where C_L and C_D are the lift and drag coefficients, respectively, C is the chord length of the 2D foil, and V_{rel} is the relative incoming velocity of the foil. The force coefficients C_L and C_D, and the chord C are read from a tabulated file. For both the AD and AL approaches, the force F_l in the momentum equation (2.2) is calculated by distributing the forces from the actuator disk/line to the background grid using the discrete delta-function approach of Yang *et al.* (2009). For more details about the formulation and numerical implementation of the discrete delta-function in turbine parametrization models, the reader is referred to Yang *et al.* (2012).

For all cases, the governing equations are discretized in space using three-point central finite differences on a hybrid staggered/non-staggered grid and integrated in time using an efficient fractional step method (Ge & Sotiropoulos 2007; Kang *et al.* 2011). To enable simulations on fine computational grids with hundreds of millions of grid nodes, we employ efficient iterative solvers with convergence acceleration techniques, such as the algebraic multi-grid method and the matrix-free Newton–Krylov method (Kang *et al.* 2011). The computer code is also parallelized using the message passing interface (MPI) to take full advantage of massively parallel computational platforms.

3. Test case and computational details

In this section, we present a brief description of the experiment of Chamorro *et al.* (2013*a*), followed by a discussion of various computational details.

The experiments were carried out in the St. Anthony Falls Laboratory (SAFL) main channel (Chamorro *et al.* 2013*a*). The channel is 2.75 m wide and 85 m long. The mean water depth (H) and mean flow velocity (U) in the channel during experiments were 1.15 m and 0.4 m s^{-1}, respectively. The channel bed and sidewalls of the main channel are hydraulically smooth rigid surfaces. Although the channel bed was initially kept clean, sand deposition zones appeared in the channel bed during the experiment, which is due to the incoming suspended sediments entering directly from the Mississippi River to the SAFL main channel inlet. Since the extent of sand deposition zones varied from place to place, no attempt was made to quantify and take into account in the simulations a representative bed roughness height for the entire channel. Assuming that the effect of bed roughness would not significantly change the characteristics of the turbine wake, we considered the bed to be smooth in all LES reported in this paper.

A model axial hydrokinetic turbine consisting of a pylon, a cylindrical nacelle and a three-bladed rotor (see figure 2*a*) was mounted on the channel bed 40 m downstream of the inlet and at the centre of the channel width. The turbine rotor diameter (D) is 0.5 m, and the centre of the rotor is positioned 0.4 m above the channel bed. The turbine is designed such that, throughout the experimental run, it can maintain constant angular velocity. The angular velocity (ω) of the rotor is 9.43 rad s^{-1} (or 90 revolutions per minute), which corresponds to a tip speed (u_ω) of 2.35 m s^{-1} and a tip speed ratio (u_ω/U) of 5.89. The Reynolds numbers (Re) based on H and U, and on D and U are 4.6×10^5 and 2×10^5, respectively; and the Froude number based on H and U is 0.12. More details of the experimental set-up can be found in Chamorro *et al.* (2013*a*). Vertical profiles of instantaneous flow velocities downstream and upstream of the turbine were measured across the channel centre using acoustic Doppler velocimetry (ADV) over a 5 min period and subsequently averaged in time to obtain mean flow and turbulence statistics.

We employ a computational domain that is $12.5D$ long, $5.5D$ wide and $2.3D$ deep in the streamwise, transverse and vertical directions, respectively (see figure 2*b*) for all LES carried out in this study. The centre of the turbine rotor and the bottom of the cylindrical pylon are located at $(0, 0.8D, 0)$ and $(0, 0, -0.3D)$, respectively. Since the streamwise distance from the inlet of the laboratory channel to the turbine ($34.78H$) is long enough to achieve fully developed flow, we assume that the incoming turbulent flow is fully developed and prescribe fully developed turbulent inflow at the inlet of the computational domain ($z/D = -2.5$). The fully developed turbulent inflow is prescribed by feeding at the inlet of the computational domain precomputed results

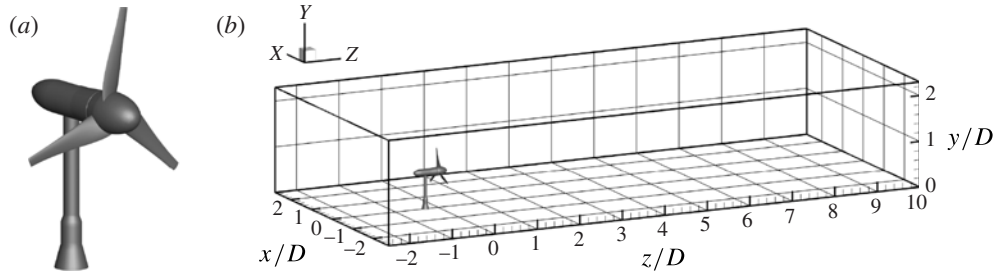

FIGURE 2. (*a*) The hydrokinetic turbine used in the laboratory experiment. (*b*) The coordinates and the location of the turbine used for the LES. The flow direction is from $-z$ to $+z$.

from a separate LES of turbulent flow in a straight open channel that has the same cross-section as the main computational domain but shorter streamwise length ($5D$) assuming streamwise periodicity. The channel bed ($y = 0$) and two sidewalls ($x/D = \pm 2.75$) are assumed to be smooth, and the near-wall modelling approach (Wang & Moin 2002) is employed to prescribe the wall shear stress boundary condition. At the free-surface boundary ($y/D = 2.3$), zero-flux and free-slip velocity conditions are imposed. For the LES-TR, boundary conditions for all three velocity components at all immersed boundary nodes in the vicinity of all turbine rotating (rotor) and stationary (pylon and nacelle) components are reconstructed using wall modelling (Kang *et al.* 2011). The axial induction factor of the turbine rotor that is required for LES-AD is calculated using the thrust force coefficient of the rotor obtained from LES-TR, which was approximately 0.9. The so-obtained time-averaged axial induction factor was 0.35. The tip speed ratio of 5.89 is used in the LES-AL.

The computational domain shown in figure 2(*b*) is discretized with a background Cartesian grid. To examine the grid sensitivity of the computed solutions, we employ two different grids for LES-TR, which are summarized in table 1. The measured friction velocity of the upstream flow is $u_\tau = 0.038$ m s^{-1} (Chamorro *et al.* 2013*a*). As a result, the wall-normal near-bed (Δy) and near-sidewall (Δx) grid spacings of grids I and II are approximately 75 and 150 wall units, respectively, and the minimum streamwise grid spacing in the vicinity of the turbine is approximately 100 and 50 wall units for grids I and II, respectively. The streamwise grid of both grids I and II was constructed in such a way that the maximum spacing in the region near the turbine ($-0.6 < z/D < 0.6$) approximately equals 190 wall units. The grid is then stretched mildly towards the downstream ($+z$) and upstream ($-z$) directions. The streamwise grid spacing in the far downstream ($z/D > 3$) and far upstream ($z/D < -2.5$) regions near the inlet and the outlet of the computational domain is set equal to 760 wall units. Grid I is also employed for LES-AD and LES-AL. To the best of our knowledge, this grid (with 100 nodes across the rotor diameter) is the finest resolution for actuator-type LES reported to date in the literature – for example, about 33, 50, 60 and 70 nodes per rotor diameter were employed in Lu & Porté-Agel (2011), Churchfield *et al.* (2012), Troldborg *et al.* (2011) and Ivanell *et al.* (2010), respectively. Grid refinement studies for the LES-AD and LES-AL, not reported herein, showed that grid I is adequate for obtaining grid-insensitive results.

For all simulated cases, the computations were first carried out until the total kinetic energy of the computational domain reached a quasi-steady state, and subsequently the flow fields were averaged for $t^* = 40$, which is equivalent to approximately 75 rotor revolution periods.

	Grid I	Grid II
$N_x \times N_y \times N_z$	$341 \times 208 \times 556$	$661 \times 392 \times 638$
Number of nodes	3.94×10^7	1.65×10^8
Near-rotor $\Delta x/D$	10^{-2}	5×10^{-3}
Near-rotor $\Delta y/D$	10^{-2}	5×10^{-3}
Near-rotor $\Delta z/D$	5.00×10^{-3}	2.50×10^{-3}
Δt^* (LES-TR)	1.07×10^{-3}	7.11×10^{-4}
Δt^* (LES-AD)	1.07×10^{-3}	
Δt^* (LES-AL)	4.00×10^{-4}	

TABLE 1. The computational grids and the time steps used for the LES-TR (grids I and II), LES-AD and LES-AL (grid I). Here N_i and Δi indicate the number of grid nodes and the grid spacing in the i direction, respectively; and t^* is the non-dimensional time defined as $t^* = tU/D$.

4. Results and discussion

In this section we first present and analyse the LES-TR results. Subsequently we present the LES-AD and LES-AL results and juxtapose the wake structure and dynamics resulting from the three approaches. All computed results are compared with the mean flow and turbulence statistics measurements of Chamorro *et al.* (2013*a*). We note that all turbulence statistics we report herein are calculated by considering velocity fluctuations about the stationary mean flow. As a result, the turbulence kinetic energy and Reynolds stresses we report in this paper contain both deterministic (due to the tip vortices, vortex shedding from tower, etc.) and turbulence contributions. Phase averaging could be used to separate these two contributions to the velocity fluctuations. Such undertaking, however, is beyond the scope of this work and has not been pursued herein.

4.1. *Turbine-resolving LES*

4.1.1. *Time-averaged flow field*

In figure 3 we compare the computed and measured flow quantities at 10 different locations along the channel centre. As seen, on both grids the LES predicts the streamwise ($\langle w \rangle$) and transverse ($\langle u \rangle$) mean velocity profiles with good accuracy. The turbulence kinetic energy (TKE; k) and the primary Reynolds shear stress ($\langle v'w' \rangle$) profiles are also predicted with reasonable accuracy. There is a slight discrepancy between the predicted and measured TKE profiles in some locations, which indicates that further grid refinements or a longer time averaging may be required. Nevertheless, the overall agreement is satisfactory considering that our LES did not introduce any *ad hoc* or empirical parameter for model calibration and we did not account for the effect of bed roughness. Overall, the comparisons in figure 3 demonstrate that the LES-TR is able to predict the flow field downstream of a hydrokinetic turbine with good accuracy.

In figure 4 we plot contours of the computed mean flow and turbulence statistics on the $x = 0$ plane. The mean streamwise velocity ($\langle w \rangle$) contours clearly illustrate that the streamwise momentum deficit induced by the turbine rotor gradually recovers as the flow moves downstream. The zero streamwise velocity contour marked by a solid line indicates that a small reversed flow region forms downstream of the turbine hub. Moreover, the transverse (azimuthal component) velocity ($\langle v \rangle$) contours show that the

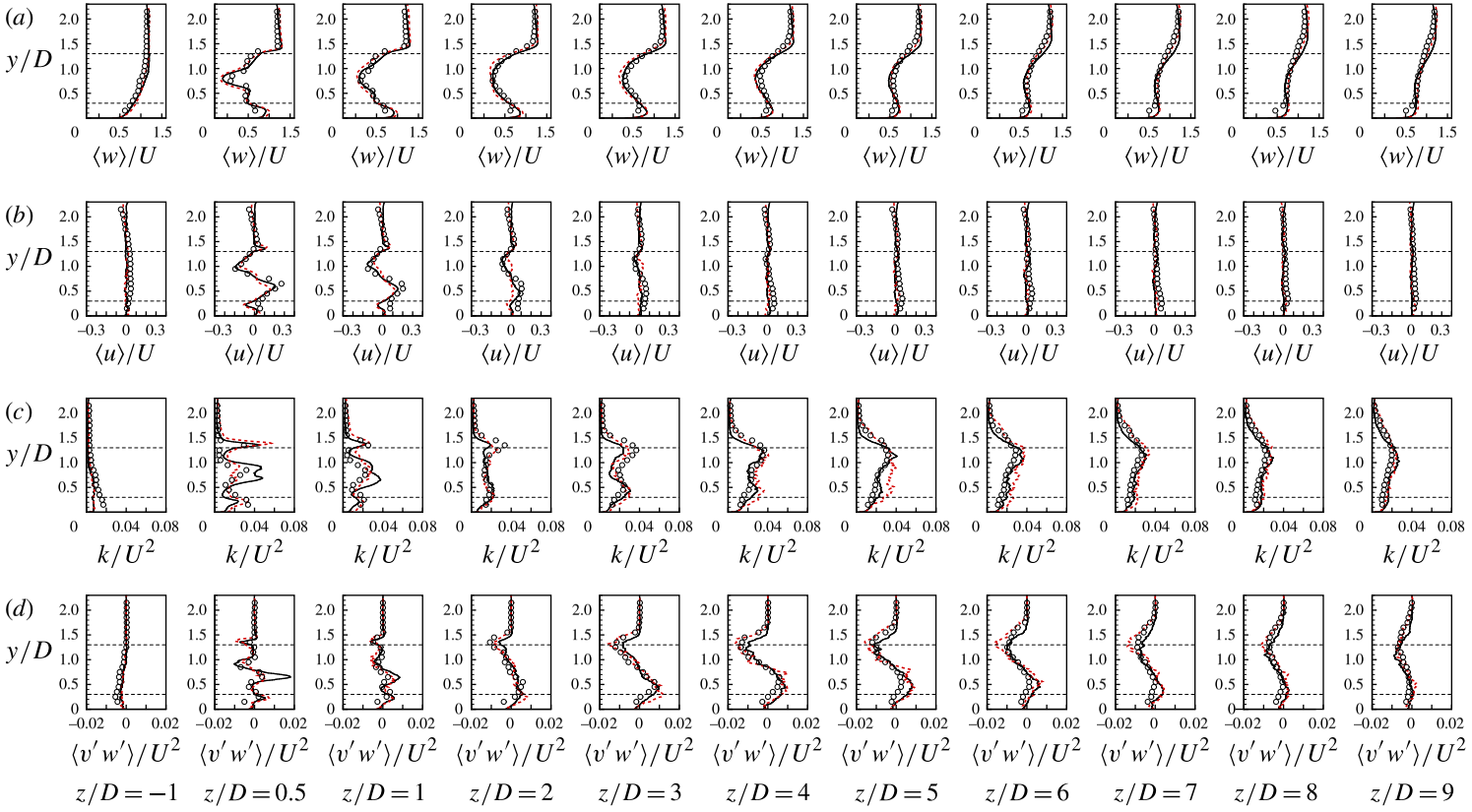

FIGURE 3. (Colour online) Comparisons of the vertical profiles of LES-TR computed (dashed line, grid I; solid line, grid II) and measured (symbols) mean flow quantities non-dimensionalized by U. The horizontal dashed lines at $y/D = 0.3$ and $y/D = 1.3$ mark the lower and upper blade tip positions, respectively. (*a*) Streamwise velocity, (*b*) transverse velocity, (*c*) turbulence kinetic energy, and (*d*) primary Reynolds shear stress. Here u, v and w are the instantaneous velocities in the x, y and z directions, respectively; the prime symbol denotes fluctuating quantities; and $\langle \cdots \rangle$ indicates the time averaging operation.

near-turbine wake consists of two counter-rotating flow regions: (i) the outer wake rotating in the same direction as the rotor blades; and (ii) the inner wake rotating in the opposite direction. The inner and outer wakes are also clearly seen in the measured velocity profiles of Chamorro *et al.* (2013*a*) (see figure 3*b*). Moreover, this complex rotational structure of the wake, and in particular the presence of the counter-rotating inner region, is consistent with Joukowski's turbine wake model (Joukowski 1912), which, for an N-blade rotor, proposes the existence of N helical tip vortices plus an additional counter-rotating hub (or root) vortex (Okulov & Sørenson 2007). The thin layers of negative and positive transverse velocity contours positioned around the upper and lower blade tip heights (see the regions where $z/D < 1$) are the footprints of blade tip vortices. The magnitude of the transverse velocity component in the inner wake becomes smaller as the flow moves downstream, and at approximately $z/D = 3$ the inner wake rotating flow almost disappears. An interesting finding is that the low-transverse-velocity region of the inner wake expands radially outwards as it gets farther downstream from the turbine. The computed TKE contours show that there are two specific locations from which pockets of high TKE emanate near the turbine: (i) around the nacelle, and (ii) the blade tips. High TKE at the blade tip heights is due to turbulence induced by the tip vortices. The existence of a layer of high-TKE regions immediately downstream of the nacelle, on the other hand, indicates that there exist shear layers around the low-velocity region within the inner wake region. It is observed that at approximately $z/D = 3$, where the azimuthal velocity becomes negligible, the two different high-TKE regions from the outer and inner wake appear to merge together and the TKE at upper tip height suddenly starts to increase downstream of this location. This phenomenon suggests that the merger or collision of the inner and outer wakes enhances turbulence mixing in the downstream wake. This trend is less pronounced in the near-bed region as compared to the upper tip region, presumably due to the effect of the channel bed. From the contours of the $\langle v'w' \rangle$ Reynolds shear stress, we can observe negative and positive $\langle v'w' \rangle$ stress regions spanning almost the entire computational domain downstream of the turbine. These regions are induced by the interaction between slow-moving fluid within the wake region and relatively fast-moving ambient fluid. There are other smaller negative and positive Reynolds shear stress regions in the vicinity of the turbine nose, which are related to the previously discussed shear layer formed around the low-velocity core near the turbine nose.

To elucidate the three-dimensional structure of the wake, we plot in figure 5: mean azimuthal velocity contours (figure 5*a*), two-dimensional mean streamlines (figure 5*b*) and TKE contours (figure 5*c*) at six cross-sectional planes (with constant z) at various distances downstream of the turbine. The thin red layers around the boundaries of the circular wake in figure 5(*a*) are the footprints of the blade tip vortices rotating in the same (clockwise) direction as the rotor, while the light blue contours indicate the counter-rotating inner wake region. Figure 5(*a*) clearly illustrates the rapid decay of the two counter-rotating wake regions at distances greater than $3D$ downstream of the turbine, where wake rotation diminishes entirely.

To better visualize the two-dimensional rotational flow structure on the cross-sectional planes, we also plot mean two-dimensional streamlines in figure 5(*b*). It is seen clearly from these figures that the entire flow within the low-velocity core rotates in the same direction as the inner wake, even though the azimuthal velocity magnitude is very small as seen in figure 5(*a*). Furthermore, the streamlines around the turbine axis suggest nearly axisymmetric rotational flow in the first two cross-sections. At the third cross-section ($z/D = 2$), we observe that the axial symmetry of the turbine

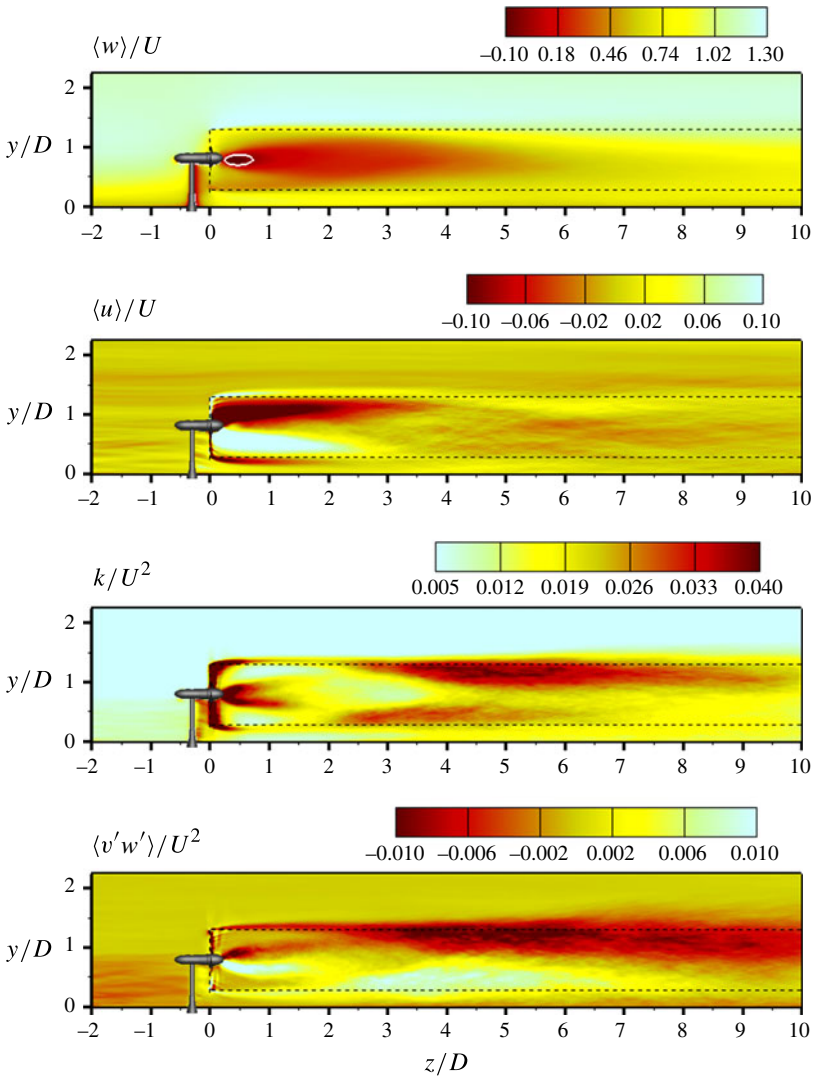

FIGURE 4. (Colour online) Contours of the LES-TR computed flow statistics at the $x = 0$ plane non-dimensionalized by the approach flow velocity U. Dashed lines indicate blade tip positions.

wake starts to disappear, and at $z/D = 3$ the streamline patterns are devoid of any axial symmetry. Multiple regions of streamwise rotation are seen to develop along the circumference of the main rotational core in figure 5(*b*) at $z/D = 2$. Further downstream, the wake undergoes another dramatic change as its rotational component starts to diminish at $z/D = 3$ and disappears completely by $z/D = 4$. As seen in figure 5(*b*), at sections $z/D = 4$ and 5 the streamline patterns suggest a sink-like flow, which entrains outer flow radially inwards towards the rotor centreline. It is important to note that the direction of the radial component of the flow is reversed somewhere between $z/D = 1$ and 2. At the $z/D = 0.5$ and 1 cross-sections in figure 5(*b*), the radial flow is directed outwards, suggesting a radial expansion of the wake. This initial trend is consistent with the streamwise momentum deficit in the immediate

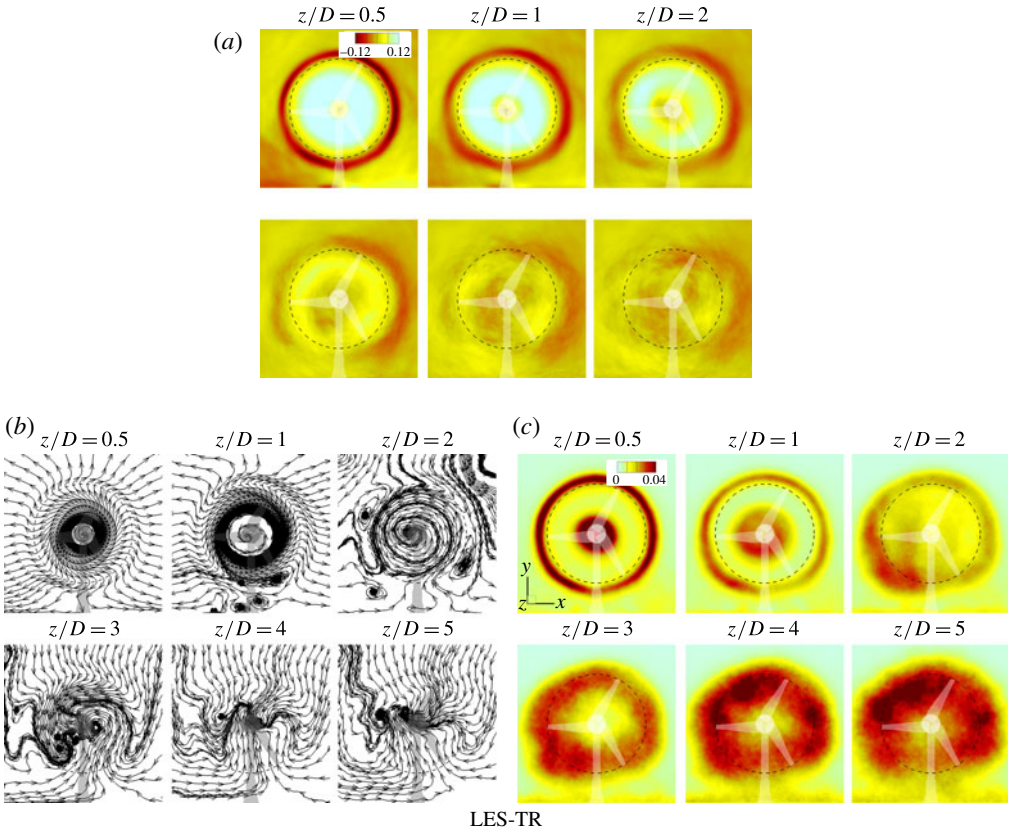

FIGURE 5. (Colour online) Contours of the computed (*a*) non-dimensional mean azimuthal velocity ($\langle u_\theta \rangle / U$), (*b*) mean streamlines, and (*c*) non-dimensional turbulence kinetic energy (k/U^2) on six different planes perpendicular to the axial flow direction. Dashed lines indicate blade tip positions. Red and light blue colors in panel (*a*) indicate the flow rotating counter-clockwise and clockwise, respectively. The rotor rotates clockwise.

vicinity of the turbine and the associated radial expansion of the stream tube outlining the rotor in order to satisfy mass conservation. Downstream of $z/D = 2$, however, the radial flow is directed inwards, suggesting transport of momentum from the outer flow towards the wake and signalling the onset of pressure recovery.

Finally, the TKE contours shown in figure 5(*c*) further reinforce what was revealed by figure 4. Namely, that the initially high-TKE regions around the outer circumference of the rotor and around the hub in the near wake diminish rapidly within two turbine diameters downstream. At distance approximately $3D$ downstream, however, an explosive growth of the TKE magnitude is observed within a circumferential crescent-moon-shaped region located radially at the outer circumference of the rotor.

It is evident that figures 4 and 5 reveal a very complex and highly three-dimensional structure of the mean wake. The most important findings from these figures can be summarized as follows: (i) the near-wake region (at distance less than $3D$ from the turbine hub) consists of two counter-rotating layers, i.e. the outer layer (turbine tip region), which rotates in the same direction as the turbine, and the inner layer, which rotates in the opposite direction; (ii) these two counter-rotating layers merge

and begin to interact with each other at approximately $3D$ downstream where the rotational component of the wake becomes negligible; and (iii) the merging of the two counter-rotating layers and the disappearance of the wake rotation are accompanied by a rapid and significant increase of the turbulence intensities and primary Reynolds shear stress along the outer tip region. Therefore, an important conclusion that emerges from our discussion of the flow physics thus far is that flow phenomena that originate in the near-rotor inner region appear to give rise to a large-scale instability of the outer wake (tip height) between $3D$ and $4D$ downstream, which presumably is responsible for the rapid increase of turbulence production seen in figures 4 and 5 in this region. In what follows, we analyse the instantaneous flow fields to elucidate the physical mechanisms that govern these complex flow patterns.

4.1.2. *Instantaneous flow fields*

Figure 6 shows the comparisons of the computed and measured power spectral density of streamwise velocity fluctuation at two locations along the upper tip height. The measured power spectral density shows that there exists a peak at approximately 4.5 Hz, which corresponds to a third of one rotor revolution, which indicates that the observed peak is the footprint of the tip vortices from the three-blade rotor. The figure shows that the strength of the tip vortex diminishes rapidly from $z/D = 0.5$ to $z/D = 1$. The computed spectral density in figure 6(*a*) shows that the LES correctly predicts the flat regions of the spectrum at low frequencies and the peak locations. The peak appearing at $z/D = 1$, however, is not predicted by the LES. These figures also show that the grid spacing of the LES is insufficient to resolve very high-frequency regions ($f > 10$ Hz). Since, however, most of the energetic turbulence motions are generated at much lower frequencies, finer-grid LES resolving higher-frequency modes should not be expected to significantly change the previously presented time-averaged result, which, even on the grid resolution we employed, are in good agreement with the measurements.

Figure 7 depicts contours of computed instantaneous streamwise velocity on the $x = 0$ and $y/D = 0.8$ planes at four different time instants spanning a period of 12 rotor revolutions. It is evident from these snapshots and video animations we have created that the low-velocity region extending along the turbine centreline downstream of the nacelle undergoes a slow precessing motion around the turbine axis. In these two-dimensional plots the precessing motion is indicated by the vertical ($x = 0$ plane) and lateral ($y/D = 0.8$ plane) flapping of the low-velocity region about the axis. This region remains coherent and clearly visible up until approximately $3D$–$4D$ downstream of the turbine. Another striking feature of the wake evident from these figures is the structure of the outer shear layer, which emanates from the turbine tips and delineates the slowly precessing, low-velocity inner core from the fast-moving outer flow. As seen in figure 7, this shear layer remains essentially confined along the imaginary cylindrical surface encasing the turbine tips up until $3D$–$4D$ downstream of the turbine. Within this near-wake region, low turbulence mixing is observed to occur across this cylindrical surface as the tip-height shear layer remains stable and essentially horizontal. Beyond this distance, however, the shear layer begins to exhibit intermittent lateral meandering motion giving rise to large-scale mixing and entrainment of fast-moving outer fluid into the central low-velocity region. Comparing figures 7(*a*) and 7(*b*) with the previously discussed figure 4, it is evident that the appearance of the pocket of high TKE along the outer shear layer at approximately $3D$–$4D$ downstream of the rotor is due to the onset of the large-scale wake meandering motions.

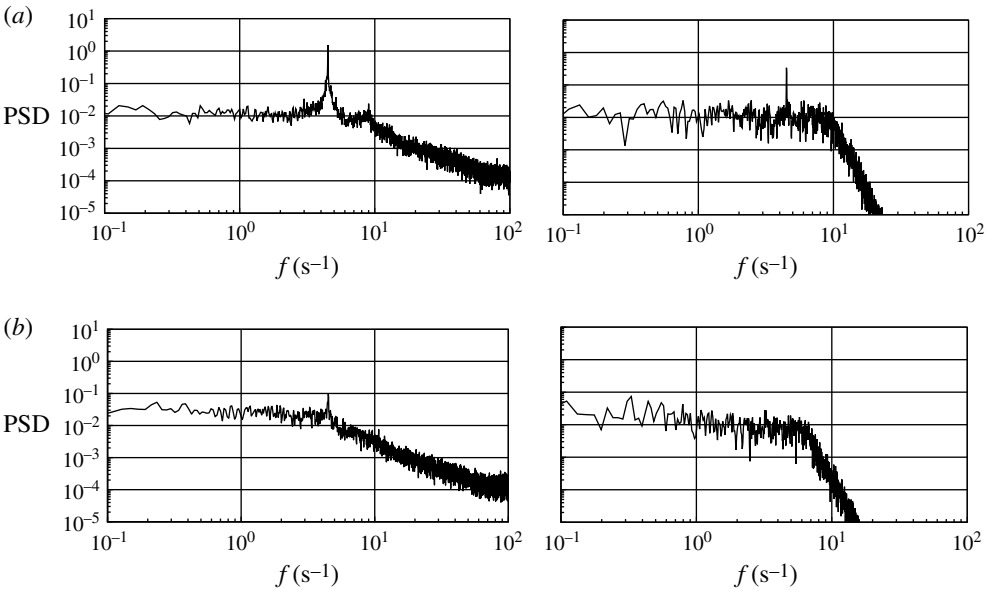

FIGURE 6. Comparisons of the measured (left) and computed (right) power spectral density at two near-turbine locations along the upper tip height ($y/D = 1.3$): (*a*) $z/D = 0.5$; and (*b*) $z/D = 1$.

The above discussion suggests that the onset of wake meandering is coupled with the dynamics of the slowly precessing inner core (hereafter referred to as the hub vortex), since this far-wake motion is triggered at approximately the same distance where the precessing hub vortex loses coherence and the overall rotational component of the wake essentially diminishes (see profiles in figure 3*b*).

To further elucidate the three-dimensional structure of the low-velocity inner core, we plot in figure 8 the instantaneous isosurface of $\langle w \rangle / U = 0.08$ at the same four time instants previously shown in figure 7. As seen, the low-velocity core emanating from the turbine nose exhibits a distinct spiral pattern. As previously indicated by the mean velocity profiles and contours shown in figures 3 and 4, the inner low-velocity region rotates in the opposite direction to the turbine rotor. By examining the details of the blade design shown in figure 2(*a*), it is evident that the junction region between the blades and the turbine nacelle will generate a swirling motion in the opposite direction to the turbine rotation. The resulting hub vortex appears to become unstable, giving rise to the slowly precessing spiral vortex core observed in figure 8.

To our knowledge, this apparent onset of the spiral mode of vortex breakdown at the hub region of an axial flow turbine has never been documented before in any previous study either for hydrokinetic or for wind turbines. This phenomenon, however, is well known to occur in a wide range of confined swirling flows spanning both laminar and turbulent flow regimes (Escudier 1988; Sarpkaya 1995). The situation that is more closely related to the present case is that of a swirl combustor where swirl is introduced in the annular region between a cylindrical pipe and a central bluff body (Al-Abdeli & Masri 2004; Syred 2006; Ranga Dinesh 2009). In this case a slowly precessing spiral vortex core has been found to form over a broad range of swirl numbers immediately downstream of the central bluff body (Ranga Dinesh 2009) and is exploited to enhance mixing and increase combustion efficiency. In our case

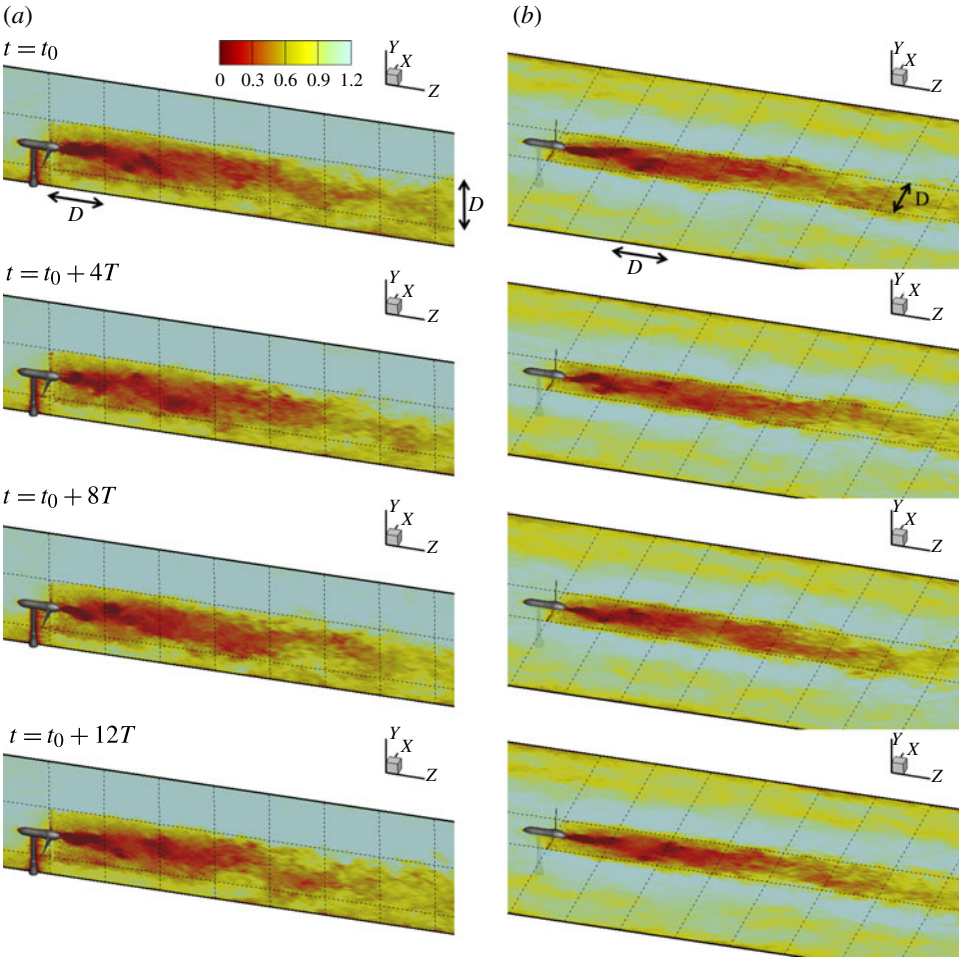

FIGURE 7. (Colour online) Contours of the LES-TR computed instantaneous streamwise velocity on the planes across the hub at four different time instants; t_0 and T indicate a reference time and one rotor revolution period, respectively.

the section of the turbine nacelle immediately downstream of the rotor acts as the central bluff body of the swirl combustor while the hub region of the turbine blades act as the swirl generator. It is thus reasonable to postulate that the details of the turbine design in this region will determine the local pressure gradients and swirl number of the hub vortex and thus dictate whether spiral vortex breakdown will occur downstream. As evident in both figures 7 and 8 (and also in the previously discussed TKE contours shown in figures 4 and 5), the region within which the hub vortex precesses spreads radially outwards from the turbine axis with downstream distance. Eventually the slowly precessing hub vortex intercepts and starts to interact with the outer shear layer at $3D$–$4D$ downstream of the rotor. Therefore, our results point to the conclusion that this interaction is a key mechanism that destabilizes the outer shear layer and augments the onset of the observed large-scale wake meandering.

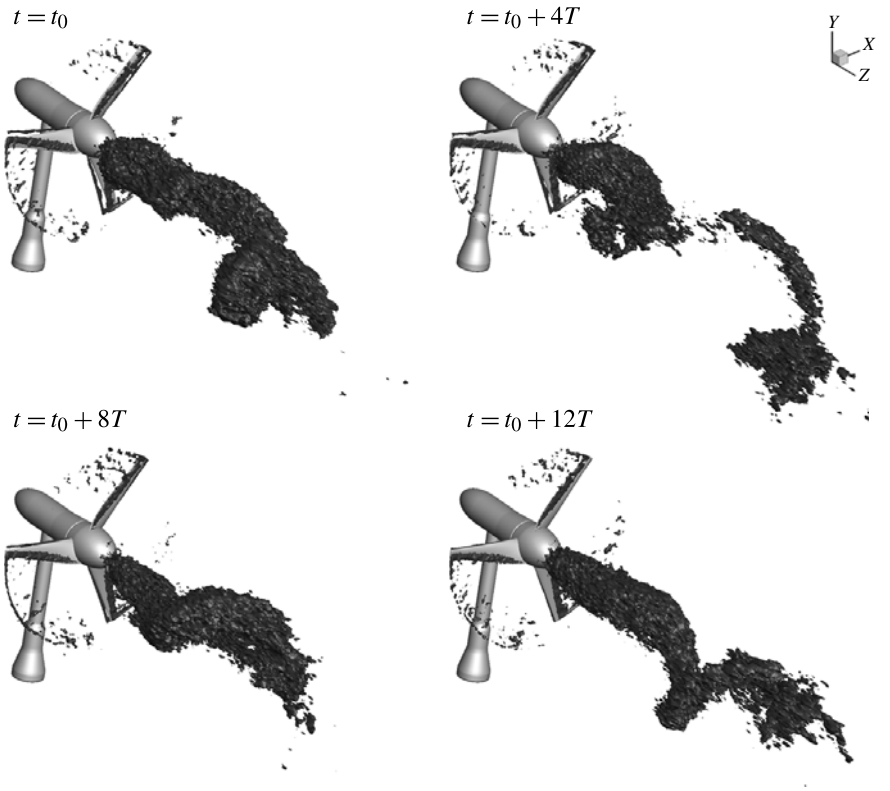

FIGURE 8. Visualization of a low-velocity LES-TR computed core downstream of the turbine. Isosurfaces of $\langle w \rangle / U = 0.08$ at four different time instants are plotted; t_0 and T are defined in figure 7.

4.2. *LES using turbine parametrization*

In this section we seek to further elucidate the physical mechanisms we uncovered in the previous section by juxtaposing the wake structure and dynamics resulting from LES-TR with those obtained using simplified parametrizations of the turbine via the AD and AL models. We seek to systematically investigate herein for the problem under consideration two important issues: (i) the uniqueness of the physical mechanism that gives rise to wake meandering in axial flow turbines; and (ii) the precise relationship between the mean flow and dynamic characteristics of wakes obtained via simplified modelling approaches (AD and AL) with those that arise in an actual turbine, which is obtained by LES-TR. For that we simplify the turbine geometry by eliminating from the model the pylon and the nacelle and considering only the turbine rotor approximated as: (*a*) a porous, non-rotating actuator disk (LES-AD); and (*b*) three rotating actuator lines (LES-AL). For both approaches, the simplified turbine models are placed in the same computational domain and exposed to the same turbulent fully developed open-channel inflow conditions as those used for the LES-TR. The LES-AD approach yields a wake without tip vortices and with no rotational component and will thus help us to clarify the wake dynamics in the absence of rotation. The LES-AL approach, on the other hand, is known to produce the effect of the tip vortices (Ivanell *et al.* 2010) but cannot be expected to capture the rich hub-vortex dynamics uncovered by LES-TR. Therefore, this approach will

help up to assess the effect of tip vortices and wake rotation but in the absence of the complex inner/outer layer dynamics.

Figure 9 shows the comparisons between the measured mean velocity and turbulence statistics profiles (Chamorro *et al.* 2013*a*) and the LES-AD and LES-AL results, respectively. As one would anticipate, given the simplicity of the AD and AL models, the overall agreement with the measurements is worse than that of the turbine-geometry-resolving (TR) LES. This trend is especially apparent in the near-wake region where the geometrical details of the turbine greatly impact the flow structure. It is evident, for instance, from figure 9 that for $z/D \leqslant 2$ both the AD and AL models are not able to resolve the low-velocity region near the hub height ($y/D = 0.8$). Furthermore, the pockets of high TKE measured around the hub height at $z/D = 0.5$ and $z/D = 1$ are either completely missing (in LES-AD) or under-predicted (in LES-AL) in the present simulations, and the TKE level near the blade tip positions is largely under-predicted especially by the LES-AD simulation. Overall, the LES-AL simulations yield better agreement with the measurements than the LES-AD, which confirms previously reported conclusions in the literature that including the tip vortices in the simulations improves the predictive capability of actuator-type models (Wu & Porté-Agel 2011). We also note that the LES-AL simulation resolves with good accuracy the structure of the swirl velocity profiles in the near wake and more specifically captures the two-layer rotating flow pattern with the counter-rotating inner region immediately downstream of the turbine hub. As previously discussed, the existence of the counter-rotating hub vortex is a direct consequence of the $N + 1$ Joukowski turbine wake model (Joukowski 1912) and therefore it should be present in any turbine model that includes rotation (Okulov & Sørenson 2007). As we will subsequently show, however, a major difference between the LES-TR and LES-AL simulations is that the hub vortex in the latter remains stable and does not develop the spiral precessing mode developed in the former.

At locations with $z/D > 3$ the agreement between both actuator-type predictions and the measurements improves markedly especially insofar as the mean streamwise velocity profiles are concerned (see figure 9*a*). This is further clarified in figure 10, which compares measured and predicted (LES-TR, -AD and -AL) mean streamwise velocity profiles along the axis of the turbine rotor ($X = 0$, $y/D = 0.8$). As seen in figure 10, both the AD and AL approaches fail to resolve the measured streamwise variation of the mean streamwise velocity component even in a qualitative sense. The agreement with the measurements improves drastically, however, for $z/D > 3$, where all three predictions begin to asymptote towards the same velocity profile. Overall, therefore, the picture that emerges from these profile comparisons is that the details of the turbine geometry near the hub region and the rich associated dynamics uncovered by LES-TR give rise to complex flow patterns in the near wake, which, as one would anticipate, cannot be resolved by either actuator-type approach. Further downstream, the predictive ability of LES-AD and LES-AL appears to improve markedly. As we will subsequently show, however, even in the far wake significant differences between the TR and actuator-based approaches do exist, which profile comparisons alone at a few locations cannot fully uncover.

Figures 11 and 12 depict the calculated TKE and primary Reynolds stress contours plotted on the turbine plane symmetry for the LES-AD and LES-AL, respectively. Comparing these two figures with similar plots from the LES-TR results (see figure 4), a number of differences become apparent. What is noteworthy, however, is that such differences are not confined only in the near-hub inner wake region, where neither actuator approach is able to capture the hub vortex dynamics and the so-induced

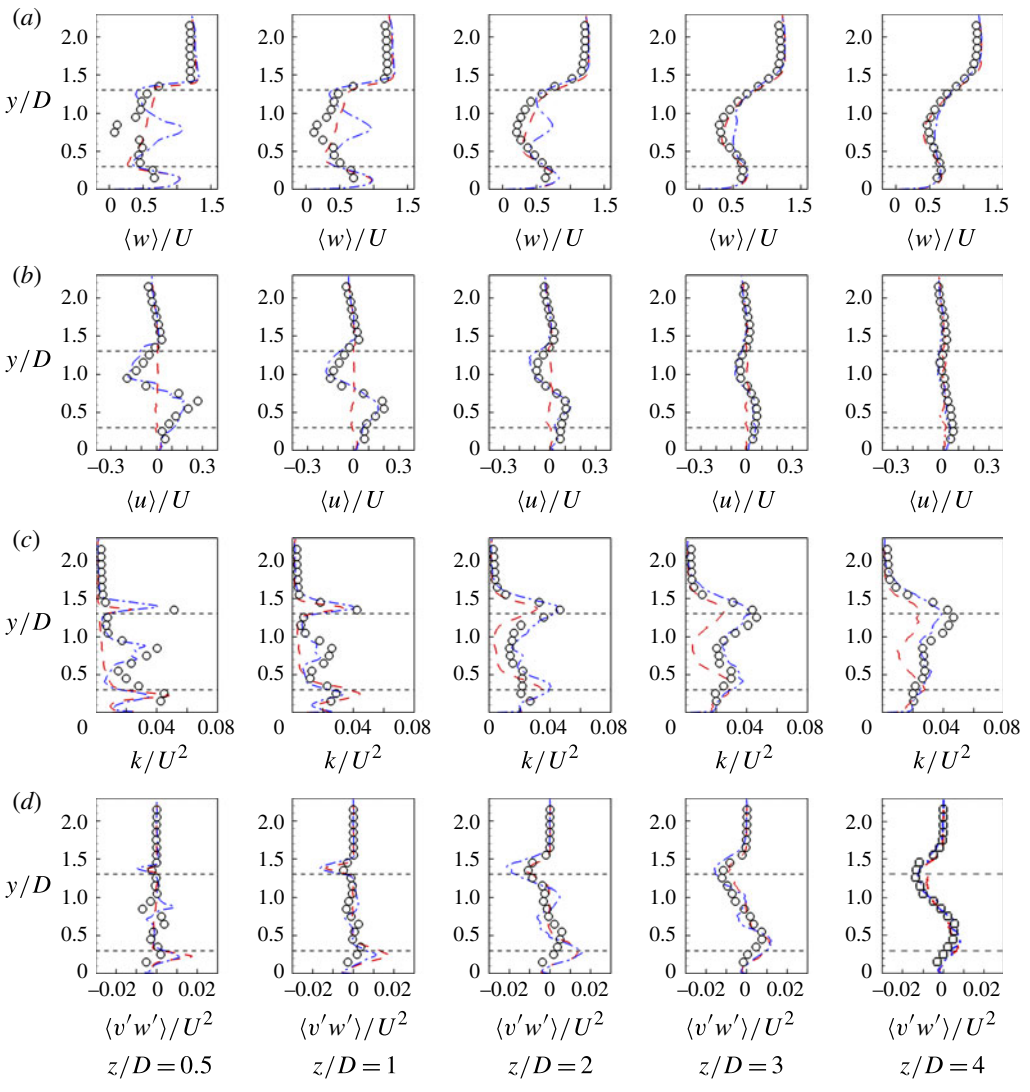

FIGURE 9. (Colour online) Comparisons of the vertical profiles of flow quantities computed by the actuator disk model (dashed line; red online) and actuator line model (dash-dotted line; blue online) on grid I (see table 1) with the measurements (symbols). (*a*) Streamwise velocity, (*b*) transverse velocity, (*c*) turbulence kinetic energy, and (*d*) primary Reynolds shear stress.

regions of high TKE and shear stress. Rather, they are also observed in the outer region (rotor tip shear layer) and persist as far as at least 10 diameters downstream of the turbine. First note that, as one would anticipate, the LES-AD model produces no high-TKE region near the turbine centreline downstream of the disk since no rotation effects are included with this model. LES-AL, on the other hand, yields a pocket of intense TKE production downstream of the turbine hub region, which is clearly associated with the counter-rotating hub vortex that is present in this simulation. As clearly evident in figure 12(*a*), however, this region of high TKE remains columnar and does not spread laterally outwards to intercept the top tip shear layer as is the

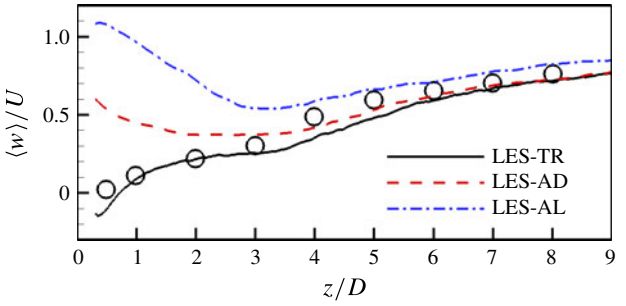

FIGURE 10. (Colour online) Comparisons of the mean streamwise velocity profiles along the centre of the rotor ($x = 0$, $y/D = 0.8$).

case in the LES-TR simulation (see figure 4). This is a major difference between the two simulations, which is due to the fact that the hub vortex in the LES-AL remains stable and does not develop the precessing spiral vortex breakdown mode observed in the LES-TR case. The reason for this is clearly evident in the streamwise velocity profiles predicted by LES-AL in figure 10. Not taking into account in the AL simulation the details of the hub geometry causes an over-prediction of the mean streamwise velocity in this region. While the intensity of the swirling motion is correctly captured by both the LES-TR and LES-AL simulations, the mean velocity profiles simulated by the LES-AL near the hub region suggest that this simulation grossly under-predicts the local swirl number, determined by the ratio of swirl-to-axial momentum. The swirl number, however, is a key parameter that governs the stability of a columnar vortex under the action of an adverse pressure gradient and determines whether vortex breakdown will occur (Al-Abdeli & Masri 2004; Syred 2006; Ranga Dinesh 2009). LES-AL does not resolve the details of the hub geometry, cannot predict correctly the deficit of axial momentum in the region, and for that yields a hub vortex that remains stable and columnar. Another important feature that is evident from figures 4, 11 and 12 is that the magnitude of the LES-TR (figure 4) computed TKE along the top tip shear layer does not increase monotonically, as is the case in both LES-AD (figure 11) and LES-AL (figure 12). Instead, the LES-TR TKE is seen to initially diminish immediately downstream of the rotor blades before it starts to grow explosively for $z/D > 3$ within the wake meandering zone. This important difference is even more evident when comparing the TKE contour plots at transverse planes, shown in figures 5, 13 and 14. Perhaps the most striking difference between the model predictions, however, is that the pockets of high TKE and (negative) Reynolds shear stress marking the wake meandering zone persist for much longer distance downstream of the turbine in the LES-TR simulation than in the two actuator models. For example, the region of high-magnitude negative shear stress in the AD and AL simulations is seen to diminish within six or seven rotor diameters downstream of the turbine (see figures 11 and 12) while for the LES-TR this zone extends up to at least 10 rotor diameters. A similar trend is also evident in the TKE contours.

To better gauge the differences in the three-dimensional structure of the various flow fields, we plot in figures 13 and 14 the LES-AD and LES-AL calculated mean streamlines and TKE contours at six different z planes, respectively. In the subsequent discussion, these figures are juxtaposed with figure 5 showing the corresponding LES-TR flow patterns. The mean streamlines show that both AD and AL models predict

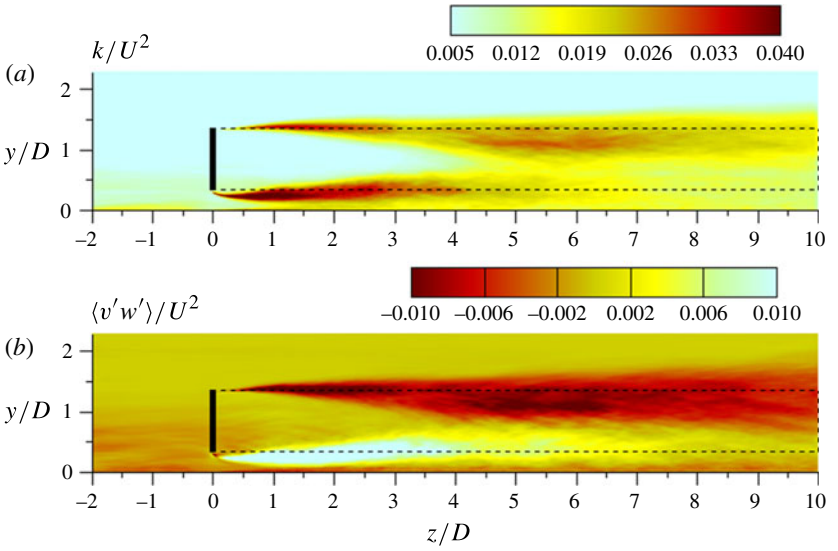

FIGURE 11. (Colour online) Contours of the flow statistics at the $x = 0$ plane computed by LES-AD using grid I. Dashed lines indicate blade tip positions.

that the radial flow reverses direction at $z/D = 2$, which is consistent with the LES-TR (figure 5). The distance required for the wake to change the radial flow direction is related to the rate of pressure recovery, which is a function of the rotor thrust coefficient and incoming flow conditions. The fact that all three models show the reversal of the radial flow at $z/D = 2$ suggests that the AD and AL parametrizations can predict the rate of wake recovery with reasonable accuracy (this is also evident from the results shown in figure 10). A major difference between the LES-AL and LES-TR flow fields is observed in the rotational flow patterns in the wake, which the LES-AD approach cannot, of course, capture at all. As seen in figure 14, in the AL simulation the rotational flow pattern in the wake remains coherent and persists for up to $z/D = 5$ and beyond (not shown herein). This trend is in stark contrast with the LES-TR results (see figure 5) in which the interaction of the precessing hub vortex with the counter-rotating outer flow causes wake rotation to essentially decay by $z/D = 4$. Another striking difference between the LES-TR and the two actuator-type models is observed in the TKE contours shown in figures 5, 13 and 14. The AD and AL models both show that the peak level of the TKE along the circumference of the rotor shear layer starts to decay for $z/D > 3$ and has diminished considerably by $z/D = 5$. Within the same region, on the other hand, the LES-TR results reveal explosive growth of the TKE, which is sustained for up to $z/D = 5$ and beyond (see figure 5).

To compare the spatial extent of the wake meandering region obtained by the TR and AL approaches, we superimpose in figure 15 the same TKE contour level on the turbine symmetry plane ($x = 0$). The selected TKE contour level ($k/U^2 = 0.03$) outlines the zones of high TKE in the computed flow fields, including the near hub, turbine tips and wake meandering regions, and succinctly captures in a single figure all previously discussed differences among the three LES results. For the LES-TR simulation we include in this figure results obtained on both grids, grid I and II (see table 1), to show that, insofar as the high TKE zone in the wake meandering region ($3 < z/D < 8$) is concerned, the two LES-TR simulations yield essentially

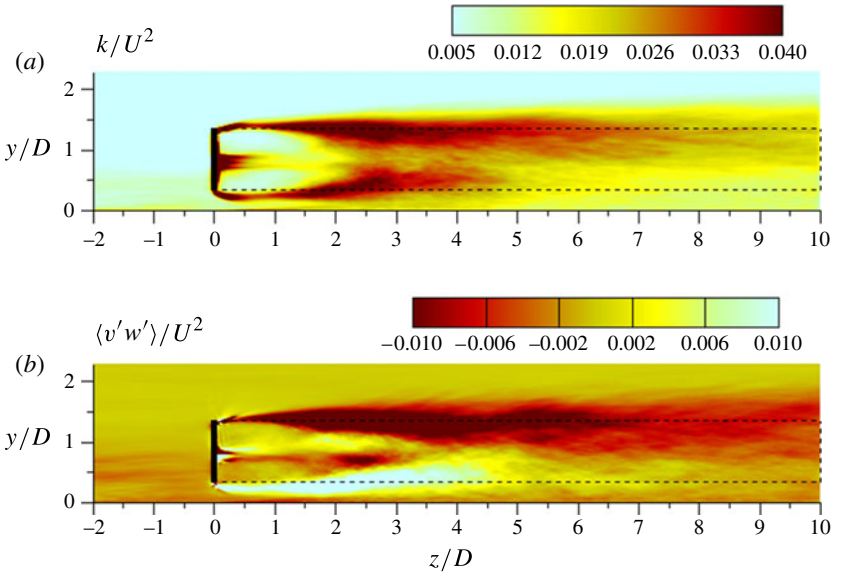

FIGURE 12. (Colour online) Contours of the flow statistics at the $x = 0$ plane computed by LES-AL using grid I. Dashed lines indicate blade tip positions.

identical results. The main difference between the two TR simulations in this regard is that on the coarse grid the wake meandering region starts closer to the turbine and as a result it is somewhat longer than that obtained on the fine grid (we will elaborate on the reason for this discrepancy in the next paragraph). As seen in figure 15, in the LES-AL simulation wake meandering is confined within a shear layer that emanates immediately downstream of the turbine top tip, starts growing in thickness at approximately $z/D = 1$, reaches maximum thickness at $z/D \sim 3.5$ and ends at $z/D \sim 5.5$. In the LES-TR flow field, on the other hand, wake meandering is marked by an elliptical-like region of high TKE levels along the turbine top tip shear layer that starts between at $z/D \sim 2.5$, reaches maximum thickness at $z/D \sim 5.5$ and extends up to $z/D = 8$. Furthermore, the maximum thickness of wake meandering region in the LES-TR flow field, which is reached where the wake meandering region in LES-AL has essentially diminished, is approximately equal to the turbine radius.

As we have already discussed above, a major difference between the TR and AL simulations is that the former is able to capture the spiral breakdown of the hub vortex whereas the latter yields a stable columnar hub vortex. To further illustrate this profound difference, we plot in figure 16 the time-averaged vorticity magnitude contours simulated with LES-TR and LES-AL. In this figure the LES-TR simulations are shown on both computational grids, grids I and II, to demonstrate that the general qualitative features of the vorticity field for this level of simulation are not sensitive to grid refinement. The distinct signature of the spiral breakdown of the hub vortex is clearly evident in both LES-TR simulations in figure 16 in the structure of the inner layer vorticity field. Two elongated layers of high vorticity forming a V-shaped pattern emanate immediately downstream of the turbine hub outlining the region within which the spiral hub vortex undergoes its precessing motion around the turbine axis. On both grids the LES-TR simulations show that this V-shaped region of high vorticity expands radially outwards and intercepts and merges with

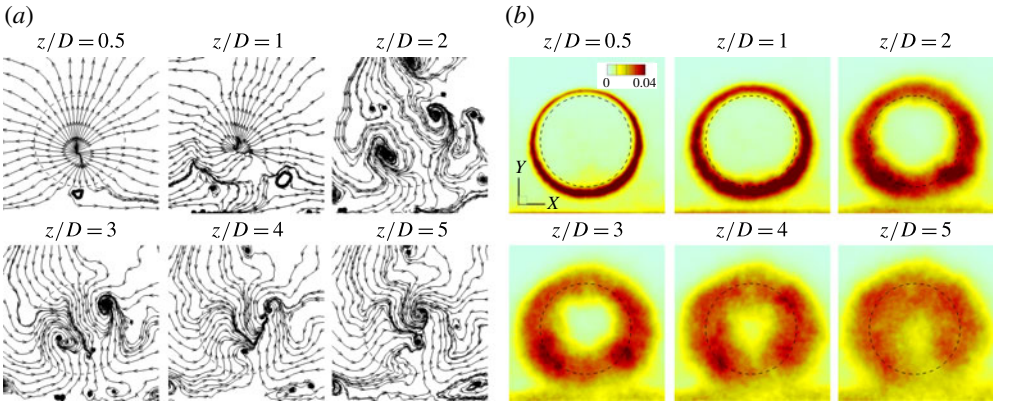

FIGURE 13. (Colour online) Contours of (*a*) mean streamlines and (*b*) turbulence kinetic energy (k/U^2) on six different planes perpendicular to the axial flow direction, which are computed by the LES-AD using grid I. Dashed lines indicate blade tip positions.

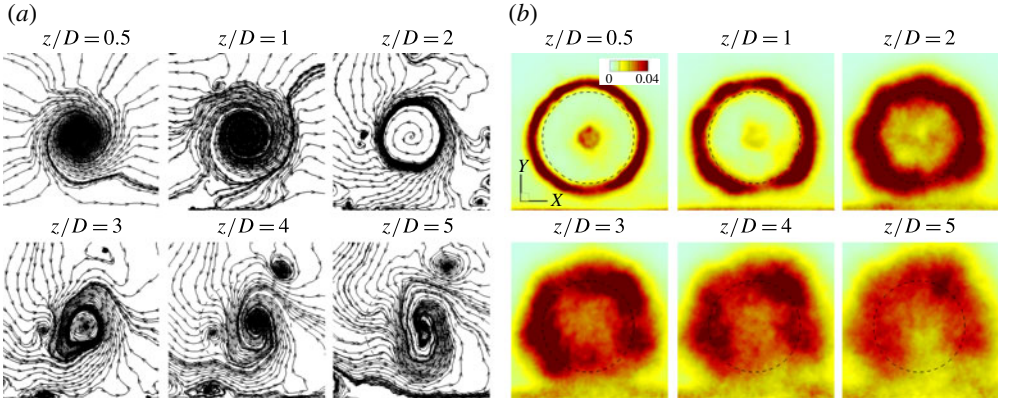

FIGURE 14. (Colour online) Contours of (*a*) mean streamlines and (*b*) turbulence kinetic energy (k/U^2) on six different planes perpendicular to the axial flow direction, which are computed by the LES-AL using grid I. Dashed lines indicate blade tip positions.

the high-vorticity region along the top tip shear layer. The main difference between the two LES-TR simulations is that on the coarse grid the inner layer vorticity expands radially faster and intercepts the outer shear layer closer to the turbine, at approximately 1.5*D*, as compared to the fine grid where this interception occurs between 2*D* and 2.5*D*. Comparing the LES-TR TKE contours shown in figure 4(*c*) with the LES-TR mean vorticity contours shown in figure 16 we note, therefore, a striking correlation between the location where wake meandering starts (the closest to the turbine end of the elliptically shaped TKE contour along the outer shear layer) and the location where the precessing hub vortex intercepts the outer shear layer. In the coarse grid the precessing hub vortex intercepts and destabilizes the outer shear layer closer to the turbine and the streamwise extent of the resulting meandering region is somewhat over-predicted when compared to that obtained on the fine mesh. This finding further underscores the main argument of this paper that the spiral instability of the hub vortex plays a major role in triggering and/or augmenting the

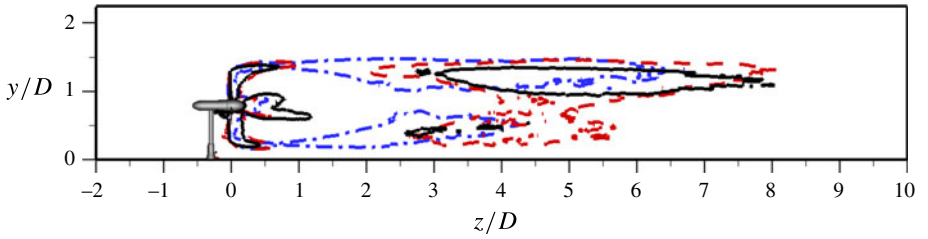

FIGURE 15. (Colour online) Comparisons of the contours of $k/U^2 = 0.03$ at the $x = 0$ plane from LES-TR (dashed lines, red online, for grid I; black solid lines for grid II) and LES-AL (dash-dotted lines, blue online).

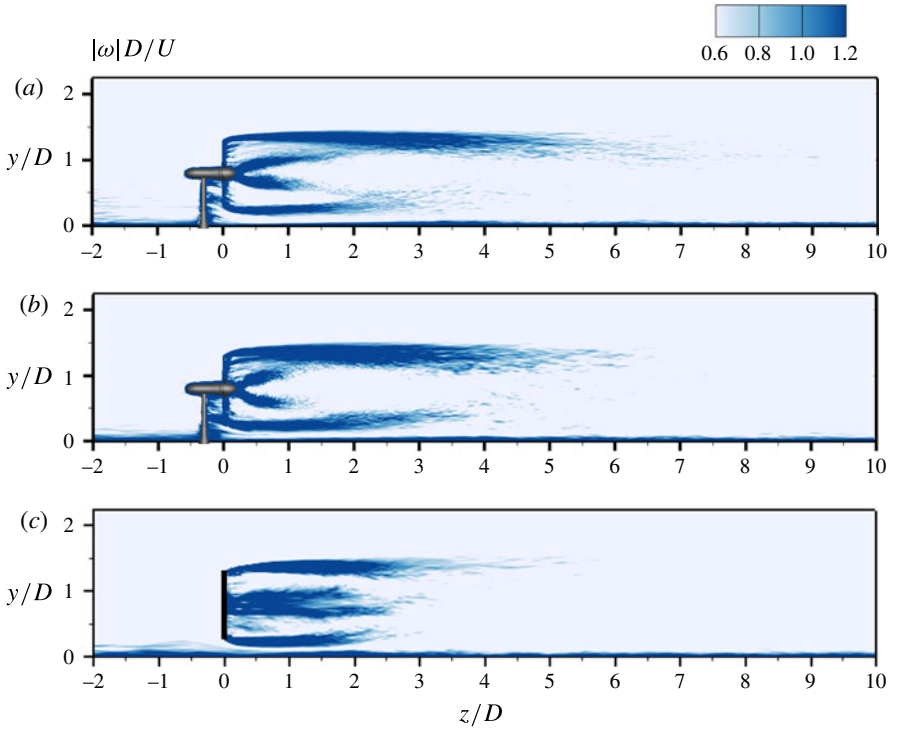

FIGURE 16. (Colour online) Contours of time-averaged vorticity magnitude at the $x = 0$ plane for (*a*) LES-TR (grid II), (*b*) LES-TR (grid I) and (*c*) LES-AL (grid I), respectively. See table 1 for the definition of the two grids.

intensity of far-field wake meandering. As does, of course, the fact that as shown in figure 17(*c*) the LES-AL simulation yields a columnar region of high vorticity in the inner layer that remains stable and never intercepts the outer shear layer. Another significant difference between the TR and AL simulations is with regard to the streamwise extent of the high-vorticity region marking the top tip shear layer. In both TR simulations large (dark blue contours) vorticity values in the outer shear layer persist up until $5D$ whereas in the AL simulation high vorticity values diminish quickly by $2.5D$. We argue that this trend is due to the fact in the TR simulations the intense interactions of the precessing hub vortex with the outer shear layer intensify vorticity generation in the outer shear layer and cause it to persist longer.

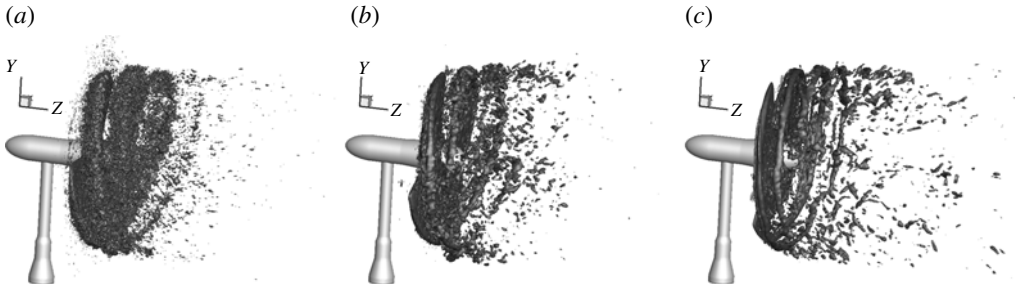

FIGURE 17. Tip vortices identified by an isosurface of vorticity magnitude for (*a*) LES-TR (grid II) $\lfloor\omega\rfloor = 26$, (*b*) LES-TR (grid I) $\lfloor\omega\rfloor = 18$ and (*c*) LES-AL (grid I) $\lfloor\omega\rfloor = 18$, respectively. See table 1 for the definition of the two grids.

The results we have discussed herein clearly show that the interaction of the hub vortex with the rotor tip shear layer has a profound impact on the wake structure and dynamics several diameters downstream of the turbine: (*a*) It modifies the mean flow by causing the wake rotation to decay completely by $z/D > 4$. (*b*) It intensifies the low-frequency velocity fluctuations within the meandering region. (*c*) It causes the region of intense velocity fluctuations to be thicker and to persist for up to eight rotor diameters downstream of the turbine. It also follows that, while both the AD and AL models yield a meandering wake, the wake structure and dynamics predicted by these models is quite different from what is observed in the wake of the actual turbine (at least for the specific turbine geometry we consider herein). In fact, the AD wake resembles more the wake of a bluff body, which is dominated by the instability of a thin shear layer and vortex shedding that originates shortly downstream of the body.

Another important conclusion from these results is with regard to the relative performance of the AD and AL models for this case. The AL model is usually considered as more advanced than its AD counterpart since it accounts for the turbine rotation effects and is able to resolve the tip vortices of the rotor blades (Wu & Porté-Agel 2011). Our results confirm this finding and show that, while both actuator-type models predict wake meandering, the LES-AL yields a considerably more extensive and intense wake meandering region than the LES-AD (see figures 11 and 12). This improved performance of the LES-AL model notwithstanding, our results clearly show that including in the turbine model the tip vortices is not, by itself, sufficient to give rise to wake meandering of the intensity and extent observed in the wake of the actual turbine. Therefore, large-scale far-wake instabilities of the tip vortices, such as those discussed by Ivanell *et al.* (2010), do not appear to be a contributing factor to wake meandering in our case. This should not be surprising since the analysis of Ivanell *et al.* assumed steady uniform laminar flow approaching the rotor, while in our case the turbine is exposed to both turbulence and mean shear due to the fully developed open channel flow we specified in our simulations. As revealed by both the LES-TR and experimental velocity spectra shown in figure 6, the strength of the tip vortices in the present flow appears to diminish rapidly within one rotor diameter downstream, which is well before wake meandering is triggered. Furthermore, in a more recent experimental study, Chamorro *et al.* (2013*b*) carried out three-dimensional three-component velocity measurements in the wake of an axial flow hydrokinetic turbine. These authors were able to reconstruct from their velocity measurements the three-dimensional structure of the tip vortices using a

vortex identification method and clearly showed that the tip vortices lose coherence and disappear completely within one diameter downstream of the turbine. Chamorro *et al.* (2013*b*) also showed that, in agreement with the present LES-TR simulations, the tangential (swirl) velocity component in the wake decays with the distance from the turbine and essentially disappears by two rotor diameters. To gauge the ability of the various models to predict the strength of the tip vortices and their experimentally observed break-up within a short distance from the rotor, we plot in figure 17 an instantaneous isosurface of vorticity magnitude for the LES-TR and LES-AL simulations. For the former we show the computed solutions on both grids I and II (see table 1). It is evident from this figure that all three simulations predict that, in agreement with the measurements of Chamorro *et al.* (2013*b*), the tip vortices lose coherence and essentially disappear within one rotor diameter downstream of the rotor. For the LES-TR simulation, this trend is identical on both the coarse and fine grids even though in the latter the tip vortices are stronger (a larger value of vorticity magnitude is plotted on grid II in figure 17) due to the significantly finer mesh resolution near the turbine. It is also worth noting from figure 17 that on the same grid resolution (grid I) the LES-AL simulation predicts tip vortices of similar strength as the LES-TR, suggesting that the AL model is able to resolve the strength of the tip vortices with accuracy comparable to that of the turbine-revolving simulation – the apparent ability of AL models to resolve tip vortices with good accuracy is consistent with a number of calculations previously reported in the literature (Ivanell *et al.* 2010; Troldborg *et al.* 2011). In summary, our computational findings along with recent experiments point to the conclusion that the presence of mean shear and turbulence in the ambient flow has a profound impact on the stability of the tip vortices. Therefore, it is reasonable to surmise that, at least for the levels of turbulence intensity present in the approach flow in this case, tip vortices cannot play a role in destabilizing the wake and inducing wake meandering. Further studies are needed, however, to better understand and quantify such impact and specifically explore the link between tip vortex stability and the turbulence levels in the ambient flow.

5. Summary and conclusions

We carried out turbine-geometry-resolving LES of turbulent flow past a hydrokinetic turbine simulating a recent experiment carried out in the St. Anthony Falls Laboratory main channel (Chamorro *et al.* 2013*a*). The comparisons of the LES-TR and the measurements demonstrate that the simulations are able to accurately predict both the near- and far-wake mean velocity and turbulence statistics. Furthermore, the computed flow field shows that the meandering of the instantaneous turbine wake is intensified considerably by the interactions of the inner wake that counter-rotates to the rotor and the outer wake due to the blade tip vortices. Specifically, the swirling flow that is set up at the turbine hub becomes unstable immediately downstream of the nacelle, with the instability manifesting itself as a slowly precessing spiral vortex core. The spiralling radius of the hub vortex grows with downstream distance and ultimately intercepts the outer shear layer close to the location where the lateral meandering of the wake is initiated. This apparent interaction of the precessing hub vortex with the outer shear layer causes the swirling flow in the wake to rapidly diminish, increases the size and streamwise extent of the wake meandering region up to eight rotor diameter downstream of the turbine, and increases turbulence mixing across the wake boundaries.

The profound effect of the energetic hub vortex on the mean flow and overall dynamics of the far wake was clearly demonstrated by carrying out LES using two

actuator-type models: LES-AD and LES-AL. While both models yielded a meandering wake, they under-predicted both the intensity of the low-frequency velocity fluctuations within and the thickness and streamwise extent of the meandering region. Our results clearly show that for both LES-AD and LES-AL flow fields the high-TKE region within the rotor tip shear layer increases monotonically immediately downstream of the turbine and that the peak TKE level has already diminished within the region where explosive TKE growth starts in the LES-TR simulation. In addition, the LES-AL flow field exhibits wake rotation that persists for many rotor diameters whereas in the LES-TR flow field the interaction of the hub vortex with the outer flow causes the wake swirl to decay completely within five rotor diameters. Therefore, our results point to the striking conclusion that, at least for our specific turbine model, taking into account the geometrical details of the turbine near the hub region is a critical prerequisite for accurately resolving the mean flow and dynamic characteristic of the far wake both qualitatively and quantitatively.

To our knowledge our work is the first to systematically investigate the predictive capabilities of actuator-type models relative to a LES model that resolves all geometrical details of the turbine. Actuator-type models are widely used today in simulations of multi-turbine arrays (or farms) because of their computational expedience and relative ease of implementation (Calaf *et al.* 2010; Lu & Porté-Agel 2011; Yang *et al.* 2012). The findings we report herein, however, regarding the under-estimation of peak TKE levels within and extent of the wake meandering region, raise some questions regarding the utility of such models as tools for optimizing layouts and spacing of multi-turbine arrays. It is worth noting in this regard that actuator-type models are typically employed with significantly coarser numerical resolution than what we have employed herein, with 100 points across the rotor diameter and over 40 million grid nodes for a single turbine calculation. This has been a major attractive feature of such models, since their ability to predict turbine wakes with reasonable accuracy using modest numerical resolution made them good candidates for modelling multi-turbine wind farms. Even though not shown in this paper due to space limitations, applying the two actuator-type models on coarser grids caused an even greater under-estimation of the extent and intensity of the wake meandering region than that obtained on the very fine, for actuator-type simulations, grid I. Therefore, future research not only should be directed towards the critical assessment of the predictive capabilities of such models but also should explore approaches for modifying them to incorporate the all-important geometry-induced near-wake dynamics revealed by the LES-TR for the present case. The challenge here will be striking a balance between modelling sophistication and computational expedience. While LES-TR is clearly not a computationally feasible approach for optimizing multi-turbine arrays, it could provide guidance for physics-based modifications of actuator-type models that can take into account near-hub flow phenomena and their impact on far-wake development. In fact the results we have presented in this paper exposed a specific weakness of the AL model, which prevented it from predicting the intensity and streamwise extent of the wake meandering region. Namely, neglecting the details of the turbine nacelle geometry causes the AL model to yield spuriously high mean streamwise velocity near the turbine centreline downstream of the hub region. As a result, the swirl number of the counter-rotating hub vortex is significantly lower than that of the vortex obtained by the LES-TR simulation, which allows the AL-predicted hub vortex to remain stable and columnar, never intercepting the outer shear layer.

Finally, it is important to note that our finding regarding the impact of the near-wake interaction of the hub vortex with the rotor tip shear layer on far-wake

dynamics is specific to the turbine geometry we considered herein. The dynamics of this interactions will clearly be affected by the specific design features of a given turbine geometry, which would determine the swirl number of the hub vortex and the near-hub pressure gradients and thus impact the hub vortex stability. Therefore, additional investigations are required to examine whether the rich near-wake dynamics we uncovered herein are also present in other turbine designs. Such investigations could also lead to physics-based strategies for designing the near-hub region of future turbines to suppress the instability of the hub vortex and thus diminish the intensity and extent of the wake meandering zone.

Acknowledgements

This work was conducted under the Advanced Water Power Project (grant number DE-FG36-08GO18168/M001) and supported by Verdant Power, US Department of Energy (DOE), National Renewable Energy Laboratory (NREL) and Sandia National Laboratories. Partial support was also provided by the US DOE (grant numbers DE-EE0002980 and DE-EE0005482), Xcel Energy (grant number RD3-42) and the University of Minnesota Initiative for Renewable Energy and the Environment. Numerical simulations were carried out using computational resources of the University of Minnesota Supercomputing Institute.

REFERENCES

AL-ABDELI, Y. M. & MASRI, A. R. 2004 Precession and recirculation in turbulent swirling isothermal jets. *Compos. Sci. Technol.* **176** (5–6), 645–665.

AUBRUN, S., ESPAÑA, G., LOYER, S., HAYDEN, P. & HANCOCK, P. 2012 Is the actuator disc concept sufficient to model the far-wake of a wind turbine? In *Progress in Turbulence and Wind Energy IV* pp. 227–230. Springer.

CALAF, M., MENEVEAU, C. & MEYERS, J. 2010 Large eddy simulation study of fully developed wind-turbine array boundary layers. *Phys. Fluids* **22** (1), 015110.

CHAMORRO, L., HILL, C., MORTON, S., ELLIS, C., ARNDT, R. E. & SOTIROPOULOS, F. 2013*a* On the interaction between a turbulent open channel flow and an axial-flow turbine. *J. Fluid Mech.* **716**, 658–670.

CHAMORRO, L. P., TROOLIN, D. R, LEE, S.-J., ARNDT, R. E. A. & SOTIROPOULOS, F. 2013*b* Three-dimensional flow visualization in the wake of a miniature axial-flow hydrokinetic turbine. *Exp. Fluids* **54** (2), 1–12.

CHURCHFIELD, M. J., LEE, S., MICHALAKES, J. & MORIARTY, P. J. 2012 A numerical study of the effects of atmospheric and wake turbulence on wind turbine dynamics. *J. Turbul.* **13** (14), 1–32.

ESCUDIER, M. 1988 Vortex breakdown: observations and explanations. *Prog. Aerosp. Sci.* **25** (2), 189–229.

ESPANA, G., AUBRUN, S., LOYER, S. & DEVINANT, P. 2011 Spatial study of the wake meandering using modelled wind turbines in a wind tunnel. *Wind Energy* **14** (7), 923–937.

GE, L. & SOTIROPOULOS, F. 2007 A numerical method for solving the 3D unsteady incompressible Navier–Stokes equations in curvilinear domains with complex immersed boundaries. *J. Comput. Phys.* **225** (2), 1782–1809.

GERMANO, M., PIOMELLI, U., MOIN, P. & CABOT, W. H. 1991 A dynamic subgrid-scale eddy viscosity model. *Phys. Fluids* A **3** (7), 1760–1765.

GLAUERT, H. 1935 Airplane propellers. In *Aerodynamic Theory* pp. 169–360. Springer.

GÜNEY, M. S. & KAYGUSUZ, K. 2010 Hydrokinetic energy conversion systems: a technology status review. *Renew. Sustain. Energy Rev.* **14** (9), 2996–3004.

IVANELL, S., MIKKELSEN, R., SØRENSEN, J. N. & HENNINGSON, D. 2010 Stability analysis of the tip vortices of a wind turbine. *Wind Energy* **13** (8), 705–715.

IVANELL, S., SØRENSEN, J. N., MIKKELSEN, R. & HENNINGSON, D. 2009 Analysis of numerically generated wake structures. *Wind Energy* **12** (1), 63–80.

JOUKOWSKI, N. E. 1912 Vortex theory of screw propeller. *Tr. Otdel. Fizich. Nauk Obshch. Lyub. Estestv.* **16**, no. 1 (in Russian).

KANG, S., BORAZJANI, I., COLBY, J. A. & SOTIROPOULOS, F. 2012 Numerical simulation of 3D flow past a real-life marine hydrokinetic turbine. *Adv. Water Resour.* **39**, 33–43.

KANG, S., LIGHTBODY, A., HILL, C. & SOTIROPOULOS, F. 2011 High-resolution numerical simulation of turbulence in natural waterways. *Adv. Water Resour.* **34** (1), 98–113.

KANG, S. & SOTIROPOULOS, F. 2011 Flow phenomena and mechanisms in a field-scale experimental meandering channel with a pool–riffle sequence: insights gained via numerical simulation. *J. Geophys. Res.* **116**, F03011.

KANG, S. & SOTIROPOULOS, F. 2012*a* Assessing the predictive capabilities of isotropic, eddy viscosity Reynolds-averaged turbulence models in a natural-like meandering channel. *Water Resour. Res.* **48** (6), W06505.

KANG, S. & SOTIROPOULOS, F. 2012*b* Numerical modeling of 3D turbulent free surface flow in natural waterways. *Adv. Water Resour.* **40**, 23–36.

KHOSRONEJAD, A., HILL, C., KANG, S. & SOTIROPOULOS, F. 2013 Computational and experimental investigation of scour past laboratory models of stream restoration rock structures. *Adv. Water Resour.* **54**, 191–207.

KHOSRONEJAD, A., KANG, S., BORAZJANI, I. & SOTIROPOULOS, F. 2011 Curvilinear immersed boundary method for simulating coupled flow and bed morphodynamic interactions due to sediment transport phenomena. *Adv. Water Resour.* **34** (7), 829–843.

KHOSRONEJAD, A., KANG, S. & SOTIROPOULOS, F. 2012 Experimental and computational investigation of local scour around bridge piers. *Adv. Water Resour.* **37**, 73–85.

LARSEN, G. C., MADSEN, H. A., THOMSEN, K. & LARSEN, T. J. 2008 Wake meandering: a pragmatic approach. *Wind Energy* **11** (4), 377–395.

LU, H. & PORTÉ-AGEL, F. 2011 Large-eddy simulation of a very large wind farm in a stable atmospheric boundary layer. *Phys. Fluids* **23**, 065101.

MEDICI, D. & ALFREDSSON, P. H. 2008 Measurements behind model wind turbines: further evidence of wake meandering. *Wind Energy* **11** (2), 211–217.

OKULOV, V. L. & SØRENSON, J. N. 2007 Stability of helical tip vortices in a rotor far wake. *J. Fluid Mech.* **576**, 1–25.

RANGA DINESH, K. K. J. 2009 Study of jet precession, recirculation and vortex breakdown in turbulent swirling jets using LES. *Comput. Fluids* **38** (6), 1232–1242.

SARPKAYA, T. 1995 Turbulent vortex breakdown. *Phys. Fluids* **7** (10), 2301–2303.

SMAGORINSKY, J. S. 1963 General circulation experiments with the primitive equations. *Mon. Weath. Rev.* **91**, 99–164.

SØRENSEN, J. N. & SHEN, W. Z. 2002 Numerical modeling of wind turbine wakes. *J. Fluids Engng* **124** (2), 393–399.

SYRED, N. 2006 A review of oscillation mechanisms and the role of the precessing vortex core (PVC) in swirl combustion systems. *Prog. Energy Combust. Sci.* **32** (2), 93–161.

TROLDBORG, N., LARSEN, G. C., MADSEN, H. A., HANSEN, K. S., SØRENSEN, J. N. & MIKKELSEN, R. 2011 Numerical simulations of wake interaction between two wind turbines at various inflow conditions. *Wind Energy* **14** (7), 859–876.

WANG, M. & MOIN, P. 2002 Dynamic wall modeling for large-eddy simulation of complex turbulent flows. *Phys. Fluids* **14** (7), 2043–2051.

WU, Y. T. & PORTÉ-AGEL, F. 2011 Large-eddy simulation of wind-turbine wakes: evaluation of turbine parametrisations. *Boundary-Layer Meteorol.* **138** (3), 345–366.

YANG, X., KANG, S. & SOTIROPOULOS, F. 2012 Computational study and modeling of turbine spacing effects in infinite aligned wind farms. *Phys. Fluids* **24** (11), 115107.

YANG, X., ZHANG, X., LI, Z. & HE, G.-W. 2009 A smoothing technique for discrete delta functions with application to immersed boundary method in moving boundary simulations. *J. Comput. Phys.* **228** (20), 7821–7836.